https://dx.doi.org/10.1016/j.ultras.2023.107176

Quantitative damage evaluation of curved plates based on phased array guided wave and deep learning algorithm

Qi Yuan[1, 3], Ying Wang[1, 4 *], Zhongqing Su[3], Tong Zhang[2 *]

1. *School of Civil and Environmental Engineering, Harbin Institute of Technology (Shenzhen), Guangdong, 518055, China*
2. *Pengcheng Laboratory, Guangdong, China*
3. *Department of Mechanical Engineering, The Hong Kong Polytechnic University, Kowloon, Hong Kong Special Administrative Region*
4. *Guangdong Provincial Key Laboratory of Intelligent and Resilient Structures for Civil Engineering, Shenzhen, Guangdong, China*

Abstract

Recent advances in phased array guided wave (PAGW) have demonstrated the potential of minor damage detection and localization in widely used curved plates, but quantitative damage evaluation remains difficult since effective features that are sensitive to damage size are hard to extract. In this study, a novel integrated framework, GW-SHMnet, is proposed, which leverages the advantages of the PAGW, finite element (FE) modeling, and deep learning algorithm. Firstly, an FE model is constructed to simulate PAGW propagation in curved plates. Secondly, PAGW experiments are performed on a curved aluminum plate to validate the FE model. Thirdly, an FE simulation database considering different sensor locations, testing frequencies, and damage sizes, is constructed and used as the training and testing data. Finally, deep learning is used to automatically extract features to determine damage size. The effectiveness, accuracy, and robustness of GW-SHMnet enable autonomous quantitative evaluation of minor damage in curved plates.

Keywords

Phased array, guided wave, deep learning, convolutional neural network, quantitative evaluation, curved plate, structural health monitoring

* Corresponding authors: Prof. Ying Wang, Harbin Institute of Technology (Shenzhen), China, yingwang@hit.edu.cn and Dr Tong Zhang, Peng Cheng Laboratory, Shenzhen, China, zhangt02@pcl.ac.cn

1. Introduction

Plate structures, especially curved ones, are broadly used in wind turbine blades, aircraft structures, etc. Considering that fatigue cracks of these curved type plates under severe operating conditions are inevitable, it is important to detect and evaluate the damage to ensure structural safety [1, 2] while reducing asset lifecycle management costs [3, 4]. Thus, structural health monitoring (SHM) in the above-mentioned engineering fields has received increasing research attention.

Since guided waves can propagate over a relatively long distance with minimum loss and are sensitive to small damages, they have found great application prospects to effectively identify the damage [5-7]. However, the interpretation of test data is still a challenging task due to the typical presence of multiple modes propagating in the test structure with different velocities and possibly interacting with each other [8]. Further, the effects of environmental and operational conditions may make the already unobvious damage reflected signal even less significant.

To overcome these challenges, phased array guided wave (PAGW) techniques have been proposed to obtain evident reflections from damage. PAGW using multiple PZT sensors arranged in a designed pattern can focus the waveform energy by predefining the focal point [9, 10]. By introducing time delays, the waveform phase of excitation signals varies. This leads to constructive interference of the emitted waves. Thus, an amplified wavefield with the desired direction appears, which can lead to magnified damage reflected waveform. By operating PZT actuators with different time delays, different focal points across the plates can be scanned, which realizes damage detection and evaluation of the plates.

Nevertheless, guided wave methods usually rely on damage reconstruction/localization algorithms, including travel time[11], diffraction tomography[12], full waveform inversion[13], and the application of different mathematical formulae to facilitate damage quantitative imaging[14-19]. A couple of deficiencies limit their wider application [20, 21]. First, the performance of these algorithms depends on manual feature selection and tuning, which means the accuracy of these algorithms is limited by the feature extraction method. Different features may yield different reconstruction accuracies in different scenarios. Second, most algorithms can only detect and locate the damage, while few can quantitatively evaluate the damage due to the complexity of signal post-processing [22-24]. Regarding curved plates, little research has been performed on the PAGW propagation characteristics earlier than our previous study [25]. In [25], not only PAGW properties of curved plates has been elaborated but also the damage detection and localization processes have been rigorously derived and

validated. It was found that the ToF (Time of Flight) and amplitude of the back-scattered CLT_0 (a mode of Circumferential Lamb Type wave) are sensitive to penetrating damage of curved plates, therefore the location of damage can be identified. However, quantitative damage evaluation, i.e., determining the damage size/level, remains a challenging task.

Quantitative damage evaluation methods of plate structures can be divided into model-based and data-driven methods. The model-based methods aim to represent the process of damage development in plate structures by constructing a theoretical/numerical model and introducing necessary variables to update the model to fit the actual scenario [26, 27]. However, the model updating process is iterative and computationally inefficient. Therefore, most model-based methods utilize numerical simulations to establish a relationship between damage parameters and signal features, i.e., curve fitting. For plate structures, the popular damage parameters include degradation of stiffness, energy dissipation of materials, etc. [28, 29]. Although this kind of method has been successfully applied in certain cases, the relationship usually lacks generalization ability and thus is difficult to adapt to different scenarios.

Compared to model-based methods, data-driven methods typically learn damage development trends from a large amount of representative sensor data and achieve damage detection and quantification without the need for physical interpretation [30, 31]. In the last decade, the fast development of GPU-based machines and the increasing availability of training data have enabled data-driven methods more viable in quantitative damage evaluation for plate structures [32, 33]. Since deep learning algorithms can learn intrinsic physics from the data without manual construction of features, they enable the structural damage/condition identification tasks to become autonomous. For example, SHMnet, a deep learning algorithm, has achieved beyond human-level performance in vibration-based damage identification tasks [34], which is promising to facilitate quantitative damage evaluation.

The successful application of deep learning algorithms relies on the availability of training data, while it is almost always impossible to gather monitoring/test data of exhaust structural conditions. A viable solution to this challenge is to simulate structural responses of representative cases with a validated numerical model, e.g., a finite element (FE) model. Its feasibility has been proved through different studies in SHM.

In the existing literature, the time delay-based PAGW technique has advantages in wavefield focusing and steering, which enables high-precision damage detection and localization in curved plates but meets difficulties in quantitative damage evaluation due to complicated signal post-processing and error-prone manual feature extraction. In such a case, deep learning can be used to automate the signal processing procedure and to improve the identification efficiency and accuracy. Therefore, in this study, a novel approach to quantitatively evaluate damage in curved plates will be proposed by combining the PAGW

technique, FE modeling, and the deep learning algorithm. To validate its efficiency and effectiveness, we compared the performance of the proposed approach with the traditional curve-fitting approach which establishes the relationship between signal feature and damage size. This paper proceeds with a description of the quantitative damage evaluation process of the proposed approach, followed by numerical simulations and experimental tests on aluminum plates based on the PAGW. Considering variables including the position of sensors, testing frequency, and width of damage, numerical datasets are constructed via FE simulations. These datasets serve not only as training/testing information for the proposed approach but also as a benchmark for comparison. Then, GW-SHMnet is developed, and its efficiency and accuracy are verified by comparing it with the results of the curve-fitting approach. This is followed by the conclusions of this paper.

2. Methodology

2.1. *Overview*

Aiming to evaluate damage size in the curved plate, we propose a new quantitative damage evaluation approach shown in Figure 1. As can be seen, the approach is composed of three stages. The first stage focuses on the PAGW. Following [25], the PA system including both Active PA and Passive PA has an ordered arc-linear array of PZT sensors bonded to the inspected structure. As the cylindrical coordinate system shown in Figure 2, the Active PA system, has 3 pieces of PZT actuators bonded to the upper surface of the curved plate, while the Passive PA system of 3 pieces of PZT sensors is bonded to the lower surface of the curved plate. By using the PAGW focusing theory for curved plates, we can obtain a wavefield in which most of its energy concentrates at the prescribed focal point, shown in Figure 3. A traditional curve-fitting approach to quantitative damage evaluation is developed, based on manual extraction of damage features and establishment of a relationship between features and damage levels, which will be used for comparison in this study.

In the second stage, FE modeling can be divided into two sub-stages. The first one is Simulations and Verification in which FE models are built and validated by experimental results. The second sub-stage is the construction of a Damage Database where wave propagation responses of the curved plates under a large amount of damage scenarios are simulated as training datasets.

For the final stage, GW-SHMnet is developed based on the architecture of SHMnet. By using the systematic simulation data as training data, three parameters, i.e., the number of convolutional blocks, the sensor location of Passive PA, and the number of training datasets are optimized. Based on GW-SHMnet, damage size can be identified through an autonomous

feature extraction and classification process. The results are compared with those of the curve-fitting approach.

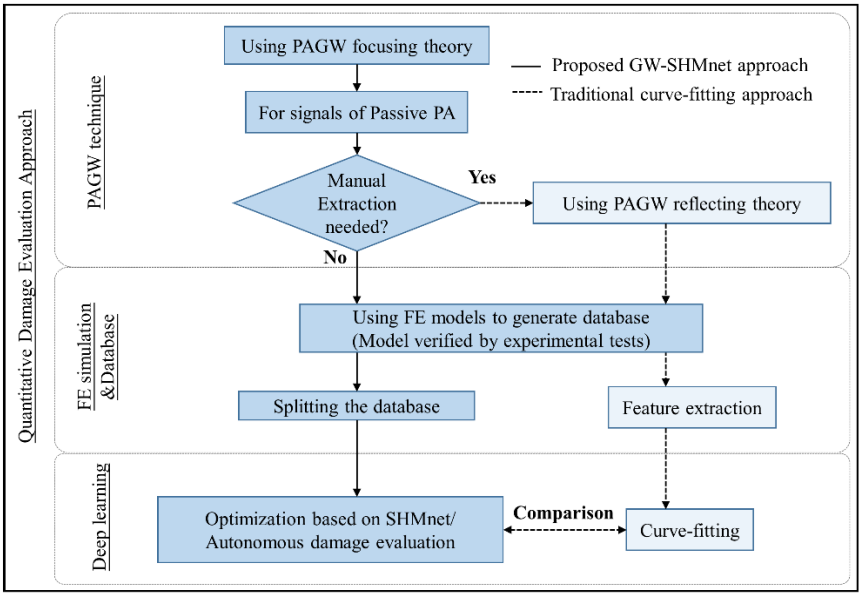

Figure 1. The proposed quantitative damage evaluation framework.

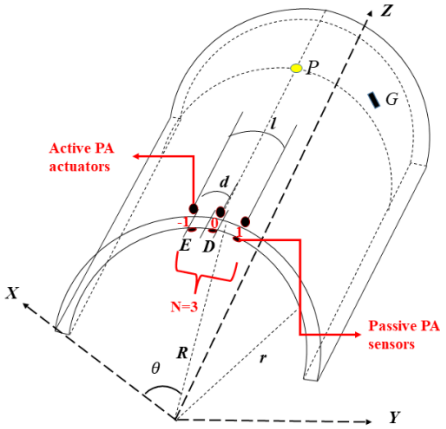

Figure 2. Diagram of curved plate model and Active PA actuators and Passive PA sensors layout in the cylindrical coordinate system.

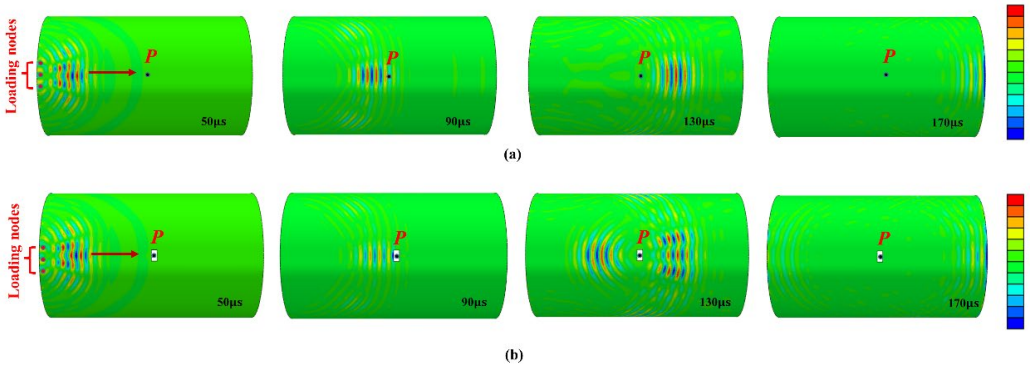

Figure 3. Example of wavefield aiming to the focal point P in (a) an undamaged curved plate; (b) a damaged curved plate[25]

2.2. *PAGW technique*

The PAGW is fundamental to the proposed approach, which includes two enabling theories. The first focusing theory is used to excite the actuators of Active PA by using prescribed signals at the same time with different phases to superimpose waveform towards the focal point. The second reflecting theory is used to synthesize the received signals from Passive PA to facilitate the extraction of the damage-reflected waveform, the back-scattered CLT_0. More details about these theories can be found in [25], while for completeness, this sub-section will provide a brief introduction.

2.2.1. The focusing theory

After defining the cylindrical coordinate system, we can know the coordinate of the focal point(P), the n^{th} PZT's coordinate, and the total number (N) of the actuators of Active PA; therefore, the distance from the n^{th} PZT actuator in the Active PA to the focal point, that is, R_n, can be determined. Assume that the amplitude of the waveform will attenuate as a function of $\sqrt{R_n}$ and group velocity of the waveform is c_g. In addition, suppose that A_n is a scalar factor to tune the amplitude of the waveform excited by the n^{th} PA actuator. Therefore, the summation of wave amplitudes at the focal point is[25]:

$$S_p(t)=\sum_{n=-(N-1)/2}^{n=(N-1)/2}\frac{A_n}{\sqrt{R_n}}\cdot S_0\left(t-\frac{R_n}{c_g}-\delta_n\right)\quad (n=0,\pm 1) \tag{1}$$

S_0 is correspond to the original excitation waveform which is then shifted using the calculated time delays. δ_n is the time delay corresponding to each actuator, which can be calculated by the following formula.

$$\delta_n=t_0+\frac{R_f}{c_g}-\frac{R_n}{c_g} \tag{2}$$

R_f is the distance from the focal point to the central actuator of the PA. t_0 is sufficiently

constant to ensure a positive time delay. After obtaining the time delay of each actuator of Active PA corresponding to the prescribed focal point, every calculated time delay is added to each excitation signal, and the PAGW propagating to the specified area of the curved plate will be observed subsequently.

2.2.2. The reflecting theory

Considering that damage exists along the propagation path of PAGW, the damage-reflected wave will appear and backscatter to Passive PA. As Figure 4 (b) shows, the sensors of Passive PA will receive signals at different times due to their distinct locations.

Suppose there is damage at G and the scattering coefficient is B. Considering the attenuation item of the reflected wave amplitude as $\frac{1}{\sqrt{G_m}}$, the signal recorded by the m^{th} sensor of Passive PA is[25, 35]:

$$S_m(t)=\sum_{-(N-1)/2}^{(N-1)/2}\frac{B}{\sqrt{G_m}}\cdot\frac{A_n}{\sqrt{G_n}}\cdot S_0\left(t-\frac{G_n+G_m}{c_g}-\delta_n\right)\quad (n,m=0,\pm1) \tag{3}$$

G_n is the distance from Damage G to the n^{th} actuator of Active PA while G_m is used to describe the distance from Damage G to the m^{th} sensor of Passive PA. M is the total number of the sensors of Passive PA. Considering the different arrival times of the received signals of Passive PA, to make the damage-reflected waveform much more significant, inverse time delays need to be manually added to the received signals. Then, we can superimpose these signals by using the same timeline, which is the synthetic signal.

$$S_R(t)=\sum_{-(M-1)/2}^{(M-1)/2}S_m\left(t+\delta_m\right)\quad (m=0,\pm1) \tag{4}$$

Given that the focal length G_f is the distance from the Damage site G to the center of the PA. The inverse time delay δ_m can be written as:

$$\delta_m=\frac{G_f}{c_g}-\frac{G_m}{c_g} \tag{5}$$

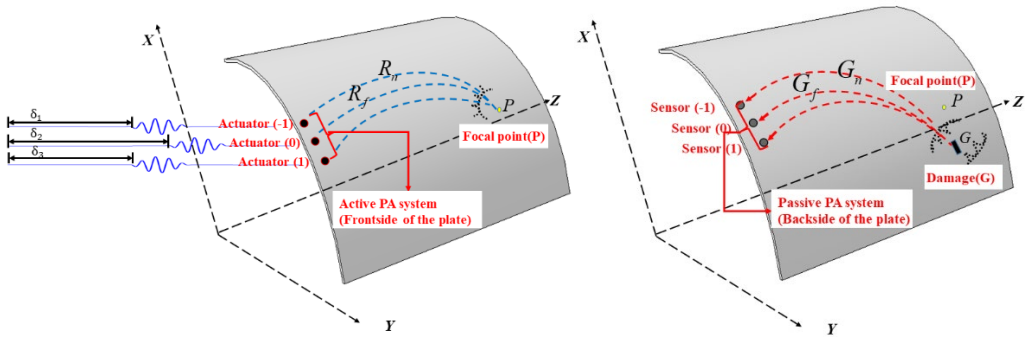

(a) **(b)**

Figure 4. Schematic diagram of curved plate PAGW technique: (a)focusing theory (b)reflecting theory.

After obtaining the synthetic baseline signal (the superimposed signals of Passive PA bonded on a pristine curved plate) and synthetic damage signal (the superimposed signals of Passive PA bonded on a damaged curved plate), the synthetic difference signal can be easily obtained by subtracting the synthetic baseline signal from the damage signal, which is the basis for the subsequent works of this research.

2.2.3. Curve-fitting approach

If there is damage on the curved plate, the damage-reflected waveform (the back-scattered CLT_0) will appear obviously in the synthetic difference signal. Since the amplitude of back-scattered CLT_0 is sensitive to the damage size, we can manually extract this parameter in the signal processing procedure and use polynomials to fit curves to describe the relationship between the damage width and the amplitude of back-scattered CLT_0. These curves can be calculated through the construction of the Damage Database and then used to predict damage size by measuring the mentioned parameter in the synthetic difference signals.

2.3. *Construction of Damage Database by using FE modeling*

In this stage, accurate and reliable numerical models need to be established. Due to their importance, the numerical simulation and experiment verification works will be presented separately in Section 3.

In this subsection, the construction of the Damage Database is introduced. Given that the FE model for PAGW has been verified by experimental tests, the FE models of curved plates with various single-site damage size scenarios can be constructed. In this study, every damage scenario is simulated by the removal of the finite elements at the damage location. Toward a more general damage identification approach, we consider 10 different damage widths. A total of 10 damaged models were built as the damage width was increasing from 5 mm to 50 mm with a step of 5 mm. Therefore, there were 10 damaged models, considering the intact plate, we have 11 models.

It has been shown experimentally that the signals received by PZT subjected to different frequencies have frequency-dependent changes such as variations in the amplitude of reflection from both damage and boundaries [36]. Considering the practical tests in engineering and the sufficient database for training, the excitation frequency used is expected to be diverse instead of the one prescribed. Therefore, we considered 9 different excitation frequencies from 90 to 110 kHz with a step of 2.5 kHz (viz. Figure 5) to implement 9 times tests for each model.

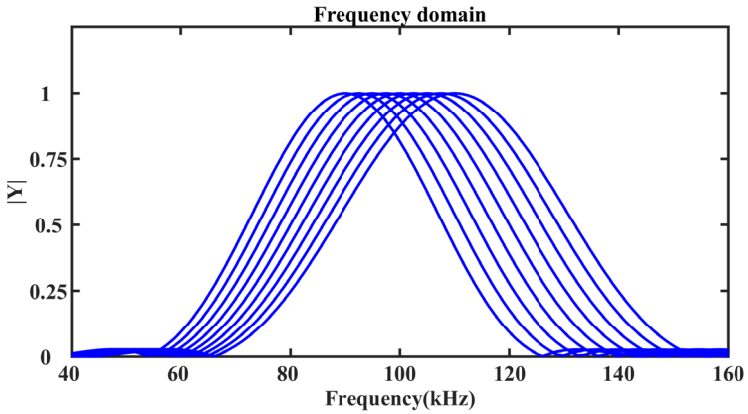

Figure 5. Excitation frequency from 90kHz to 110kHz with a step of 2.5kHz

For the database of the proposed quantitative damage evaluation approach, there is no need to manually extract damage indicators of the recorded signals of Passive PA. After simulation, all the signals received by Passive PA (3 sensors) are directly reordered to create 3 groups of datasets, one for each receiver (sensor), comprising simulated measurements from 11 different damage scenarios (model), where 9 excitation frequencies were implemented for each model. In total, we have 3*11*9=297 simulation datasets.

For each sensor (99 datasets), we used an increasing number of numerical dataset groups as training data to study the effect of the number of training datasets, that is, Group 1 to Group 5 (viz. data group in Table 1). Considering that there are always 11 damage width scenarios at each excitation frequency, 'Group 5' means that a total of 55 test results were used for training. The rest datasets of '92.5 kHz', '97.5 kHz', '102.5 kHz', and '107.5 kHz' were always used as testing data in the following training processes.

Table 1. Description of training data and Testing data

Datasets	Group Number	Excitation frequency scenarios				
Training data	Group 1	90kHz	-	-	-	-
	Group 2	90kHz	95kHz	-	-	-
	Group 3	90kHz	95kHz	100kHz		-
	Group 4	90kHz	95kHz	100kHz	105kHz	-
	Group 5	90kHz	95kHz	100kHz	105kHz	110kHz
Testing data	-	92.5kHz	97.5kHz	102.5kHz	107.5kHz	-

Note: Each excitation frequency scenario corresponds to 11 damage scenarios.

2.4. *Deep learning algorithm*

SHMnet is a novel deep convolutional neural network for SHM, proposed by Zhang et al. [34], which was adapted from a state-of-the-art network configuration, Alex-Net, together with Adam's optimization algorithm. In this study, optimization of SHMnet's network architecture is implemented towards better performance and efficient training and testing in the context of PAGW. The parameters including the number of convolutional blocks, the PA sensor's location, the number of training datasets, and the training data preparation scheme, have been optimized.

After parameters optimization, the trained GW-SHMnet model will be used to classify the damage width label. Once the received signals of Passive PA are inputted to GW-SHMnet, features can be extracted automatically and damage size will be classified and identified. The algorithm will autonomously calculate the testing (classification) accuracy and give the results, which means that the quantitative damage evaluation process can be achieved.

GW-SHMnet consists of two main parts, i.e., Feature extraction and classification, shown in Table 2. The feature extraction part has three one-dimensional convolutional layers with kernel sizes of 7, 5, and 3, which is followed by nonlinear ReLU activation and maximum pooling with a kernel size of 3 and a step size of 2. The classification part is combined by two ReLU layers, two dropout layers, each with a ratio of 50%, and three dense/fully connected layers, which convert the learned features to a total number of output classes that can be adapted to different scenarios. We set this number as 11 for a total of 11 damage scenarios considered in this study. According to previous related research results, we set the learning rate as 0.0001 and the training epochs as 1000.

Table 2. GW-SHMnet network architecture [34]

Network architecture
(Feature extraction): Sequential ((0): Conv1d (1, 16, kernel_size = (7,), stride = (1,)) (1): ReLU(inplace) (2): MaxPool1d (kernel_size = 3, stride = 2, padding = 0, dilation = 1, ceil_mode = False) (3): Conv1d (16, 64, kernel_size = (5,), stride = (1,)) (4): ReLU(inplace) (5): MaxPool1d (kernel_size = 3, stride = 2, padding = 0, dilation = 1, ceil_mode = False) (6): Conv1d (64, 256, kernel_size = (3,), stride = (1,)) (7): ReLU(inplace) (8): MaxPool1d (kernel_size = 3, stride = 2, padding = 0, dilation = 1, ceil_mode = False))
(Classification): Sequential ((0): Dropout (p = 0.5) (1): Dense (in_features = 158976, out_features = 1024, bias = True) (2): ReLU(inplace) (3): Dropout (p = 0.5) (4): Dense (in_features = 1024, out_features = 1024, bias = True) (5): ReLU(inplace) (6): Dense (in_features = 1024, out_features = 11, bias = True))

3. Numerical simulation and experimental verification

In this section, the construction of numerical models will be described, and the effectiveness of numerical simulations will be verified by experimental results.

3.1. *Dispersion curves and the excitation signal*

Due to the inherent properties of guided waves, e.g., multi-modes and dispersion, it is vital to choose an appropriate excitation frequency according to dispersion curves to limit excited

wave modes. Following previous studies [25, 37, 38], we can calculate the dispersion curves of the circumferential lamb type (CLT) wave. Figure 6 shows the curves in terms of group velocity for different frequency-wall thicknesses when the curved plate with a ratio of its radius to wall thickness is greater than about 20. Because of the radius of curved plates, it is difficult to distinguish symmetric and anti-symmetric modes. Thus, the subscript m in CLT_m is used to designate the wave mode number. By inspecting Figure 6, we decided to conduct experiments using the fundamental CLT_0 mode at 0.4 MHz.mm, for which limited dispersion is expected due to the derivative of its group velocity being close to zero at the chosen frequency. A similar choice would be commonly made in the simulation since it reduces the complexity of the signal analysis by limiting the number of modes excited in the test structure.

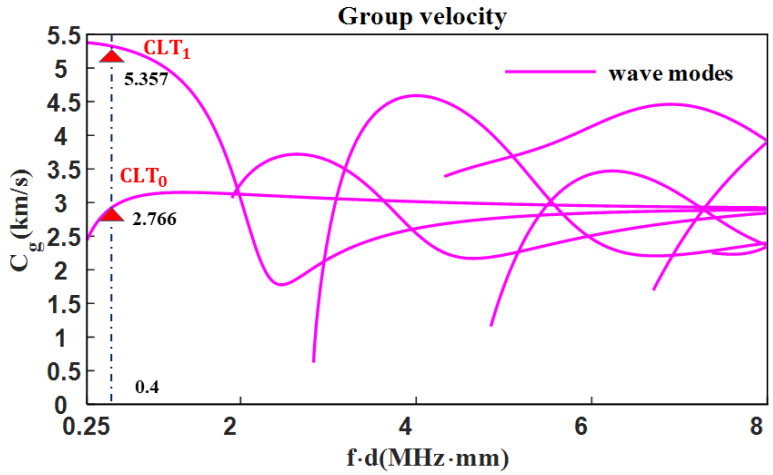

Figure 6. Dispersion curves of CLT waves in an aluminum plate in group velocity.

3.2. *Numerical simulation*

To build FE models, a 3D model of a 400×400×4 mm curved type aluminum plate with a radius of 250 mm was first created with commercial software, ABAQUS, which can perform explicit time-domain simulation of wave propagation efficiently. To create a damaged plate, a through-thickness rectangular puncture damage was introduced at the desired nodal location by removing elements. Three actuators of Active PA were simulated by selecting the nodes on the left edge of the upper face of the plate, which were assigned to excite a force time-history with the shape of a 5-cycle, Hanning windowed tone-burst at 100 kHz shown in Figure 7 (a); the force was directed normally to the plate, hence predominantly exciting the CLT_0 mode and only to a much lesser extent the extensional CLT_1 mode. Furthermore, Passive PA is simulated by selecting the nodes on the right edge of the lower face of the plate and by recording the displacement time history at the node in the normal direction to the plate for each simulation step [39, 40]. Overall, this provides a reasonable simulation of the stress waves that would be excited and sensed by small piezoelectric discs attached to the plate. Aluminum was modeled as an isotropic non-attenuative material whose density, elastic modulus, and Poisson's ratio

were set based on literature value. This time, a damage width of 20 mm was considered, and the length of damage was set as 10 mm. All the parameters are shown in Table 3.

Table 3. Parameters of the curved aluminum plate and the information of damages.

Item	Density [kg/m^3]	Modulus [Mpa]	Poisson's Ratio	Radius[mm]	Width [mm]	Length [mm]	Thickness [mm]	Damage width [mm]	Damage length [mm]
Value	2700	69000	0.33	125	400	400	4	20	10

The simulation time-step of 25ns was chosen to satisfy the precision and stability requirements typical of elastodynamic simulations. It was recommended to use at least 10 elements per shortest propagating wavelength to guarantee accuracy [41]. According to the group velocity shown in Figure 6, for 100kHz, the minimum wave velocity of the guided wave is 2766m/s at 0.4 MHz · mm, and thus the maximal edge length of the elements is 2.766 mm [25]. While for 110 kHz, the calculated maximal edge length of the elements is 2.566 mm and 2.999 mm for 90 kHz. Therefore, considering the calculation results and efficiency of the simulation, the mesh grid size is set to 2.5mm in 11 models. The simulation duration was set to 0.5 ms as the CLT_0 wave mode can propagate for about 1.4 m from Active PA. This duration is sufficient for the damage reflection and multiple reflections from the plate boundaries to reach either of Passive PA.

3.3. *Experimental setup*

To verify the effectiveness of numerical simulations, experimental works on type-6061 thin curved aluminum plates with a size of 40 cm by 40 cm by 4mm and a radius of 250 mm were performed. The material parameters of the aluminum and excitation signal are the same as those in numerical simulations. As shown in Figure 7, each three disk-shaped PZTs of 1 mm thickness and 10 mm diameter were used for Active and Passive PA, with a distance of 23.4 mm between the PZTs, taking care to ensure that the time delay between waves excited by adjacent PZT actuators is always an integer multiple of 0.5 microseconds, the minimum sampling interval of the NI PXIe-6124. The signal is excited by an active amplifier and recorded by a passive amplifier at a sampling rate of 2 MHz.

The high-speed acquisition system together with Active PA and Passive PA is shown in Figure 8(a). As Figure 8(b) marked, C (250, 0.8, 200) is the focal point set at the center of the plate, and the time delays were t_1=0, t_2=0.5, and t_3=0 μs between Active PA actuators. A total of three analog output channels were used on the data acquisition cards to control three actuators of Active PA. The excitation signal for each analog channel is supplied with a maximum of 150 V via a PINTECH high-voltage amplifier, HA-405 or HA-820. In addition, the charge signal output from Passive PA was converted to a voltage signal using the DONGHUA charge

amplifier and subsequently recorded on LabVIEW using the three analog input channels of PXIe-6124. Besides, the charge amplifier has an internal integrated bandpass filter with a bandwidth of 30kHz to reduce noise outside the signal bandwidth.

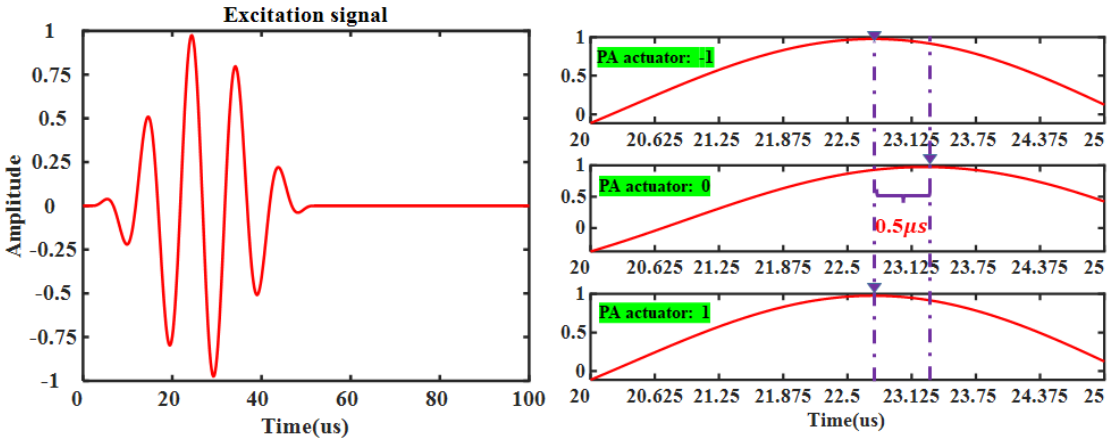

(a) (b)

Figure 7. (a)Excitation signal in the time domain; (b) Time delays of Active PA actuators

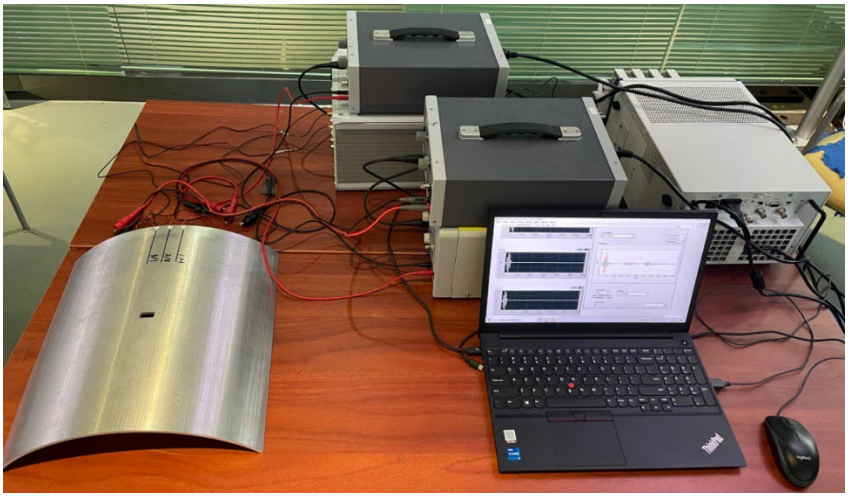

(a)

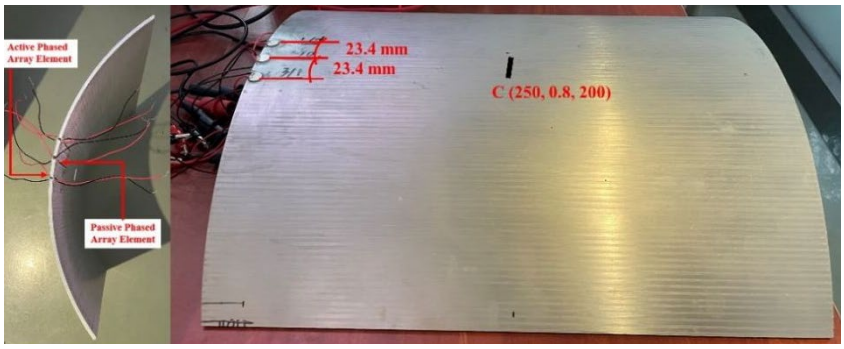

(b)

Figure 8. (a) PA system hardware and software are designed for health monitoring of plate structure; (b) PZT locations and measurement lengths annotation.

3.4. *Simulation and experimental results*

The time delays in numerical simulations are set the same as that in the experiment, and the PAGW propagation properties are studied in the pristine and damaged curved plate models. As mentioned before, the CLT_0 and CLT_1 modes should exist in the wavefield, which can be reflected from the damage and the boundaries at different times according to their different velocities as Figure 9 shows. For the plates with a radius of 250mm, synthetic signals of damaged and healthy scenarios in response to the same excitation are plotted in Figure 9 (a). For the synthetic difference signal, CLT_0 backscattered from the damage is present, which is plotted in Figure 9 (b).

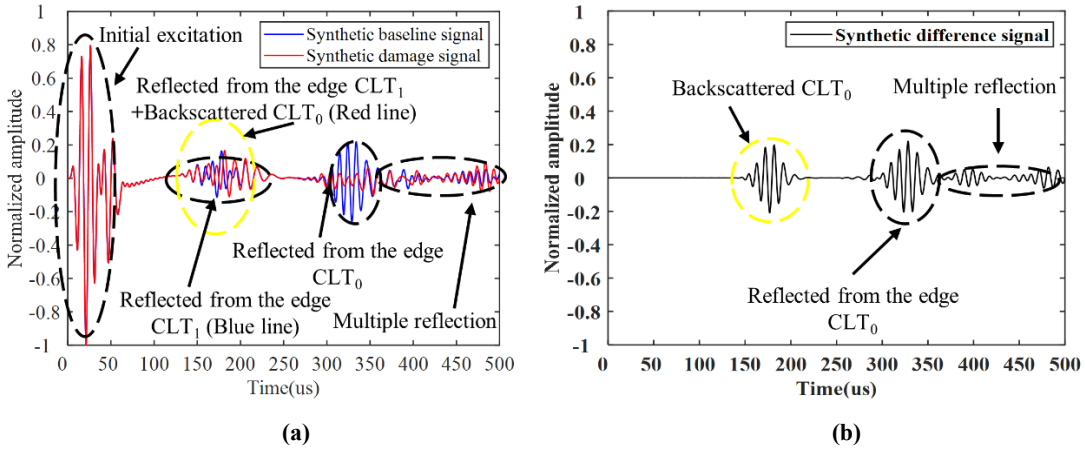

Figure 9. (a) Synthetic signals of Passive PA in both undamaged(baseline) and damaged plates with a radius of 250 mm in the simulation; (b) Synthetic difference signal calculated from Synthetic damage signal and baseline signal.

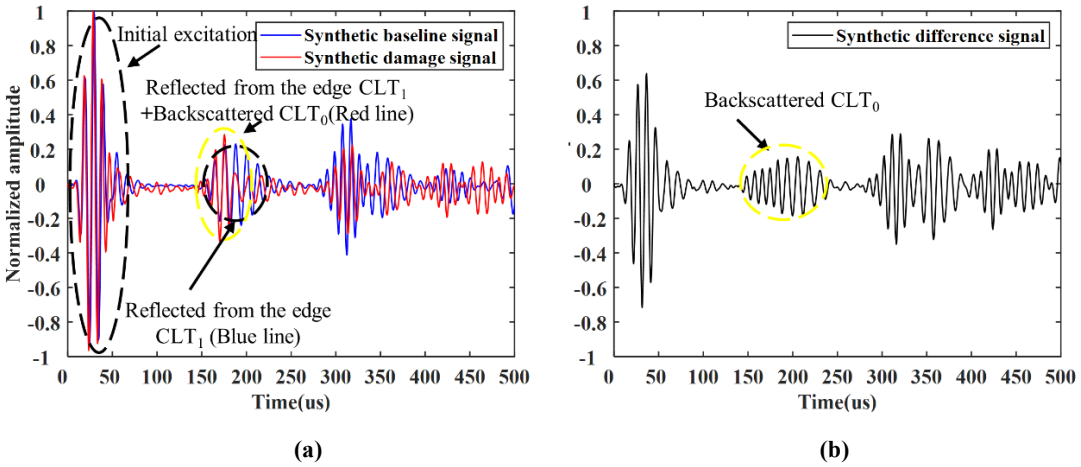

Figure 10. (a) Synthetic signals of Passive PA in both undamaged(baseline) and damaged plates with a radius of 250mm in the experiment; (b) Synthetic difference signal calculated from Synthetic damage signal and baseline signal.

As for experimental results, Figure 10 (a) shows synthetic signals for both the pristine and the damaged curved plates in experimental tests. In Figure 10 (b), the responses from the

damaged curved plate have a strong damage-reflected waveform which can be called back-scattered CLT_0. To verify the FE models of curved plates, the experimental results of the PAGW can be compared with the numerical simulation results. Comparing Figure 10 (b) with Figure 9 (b), we can find that all the back-scattered CLT_0 signals of both simulation and experiment are in the period of 150-200 μs with a max amplitude of around 0.2. Although there are inevitable noises in the experiment's results, the main features of backscattered CLT_0 were not greatly affected. Together with the results of the previous work for 125mm curved plates [25], which obtained synthesized signals with a low extent of noise wave and calculated travel time/amplitude of backscattered CLT_0 were very close in both experiments and simulations, demonstrate the effectiveness and accuracy of FE model that can be used to simulate the propagation of PAGW and thus generate data for other scenarios as a database.

4. Quantitative damage evaluation

After the verification of FE modeling and the generation of the Damage Database, we use this database to optimize SHMnet and compare the results with those using the conventional curve-fitting approach.

4.1. *Optimization and quantitative evaluation results of GW-SHMnet*

In this work, we normalized the received signal of each recording node of Passive PA according to its maximum amplitude. Considering computing efficiency, we re-sampled the data to 5000 points each. Besides, we labeled the data from the different sensors of Passive PA under different damage size scenarios with their associated scenario numbers, which are ready to be used for training. Moreover, the normalized datasets and their associated labels were utilized to optimize SHMnet for the following three parametric studies. After that, we used a different Group of datasets from one sensor of Passive PA under all scenarios as the training data. The trained GW-SHMnet model was then used to identify the damage width label with 'unknown' scenarios by using the selected testing datasets. If the correct damage size scenario label was found, we considered the result accurate, and vice versa.

4.1.1. Effect of the number of convolutional blocks

To find the optimal number of convolutional blocks, we first implemented parametric studies on five modified SHMnet networks with 1, 2, 3, 4, and 5 convolutional blocks, respectively. We used 'Group 5' testing data from sensor 0 in Passive PA as the training data, thus 55 datasets were used in total. As shown in Figure 11, the network with 3 convolutional blocks achieved the best training and testing accuracy, that is, 100%. With fewer convolutional blocks (1 or 2), the network tends to be under-trained, where the training accuracy is only 92%

and less than that of testing accuracy. With more convolutional blocks (4 or 5), both the testing accuracy and the training accuracy are lower than those with 3 convolutional blocks. Therefore, 3 convolutional blocks are found to be optimal for this study and used thereafter.

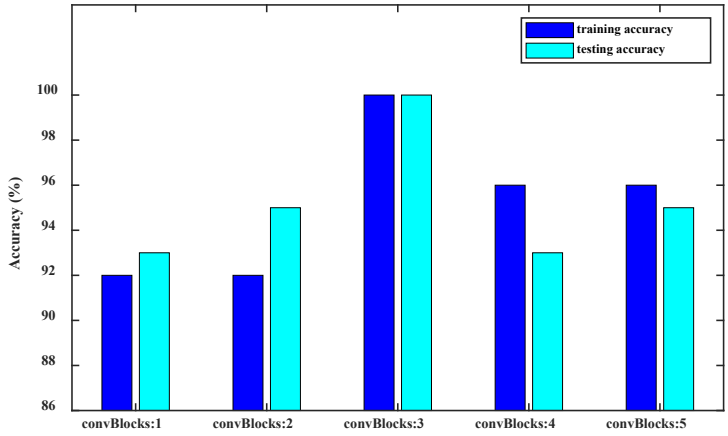

Figure 11. Comparison of training and testing accuracy of SHMnet with different numbers of convolutional blocks.

4.1.2. Effect of PA sensor's location

Then, we investigated the effects of the Passive PA sensor's location on the accuracy of SHMnet. We used 'Group 5' data from three sensors as three sources of training data. With each training data source, SHMnet would be trained and used for quantitative damage evaluation. The training and testing accuracy results of using sensor data at different locations of Passive PA sensors are shown in Figure 12. It can be seen that the algorithm can achieve 100% quantitative evaluation training and testing accuracy by using any data from Passive PA sensors -1, 0, and 1. Therefore, data from any sensor of Passive PA can be used for quantitative damage evaluation, as long as it is consistent during training and testing. In the rest of the parametric studies, we select the data from sensor 0 as the training data.

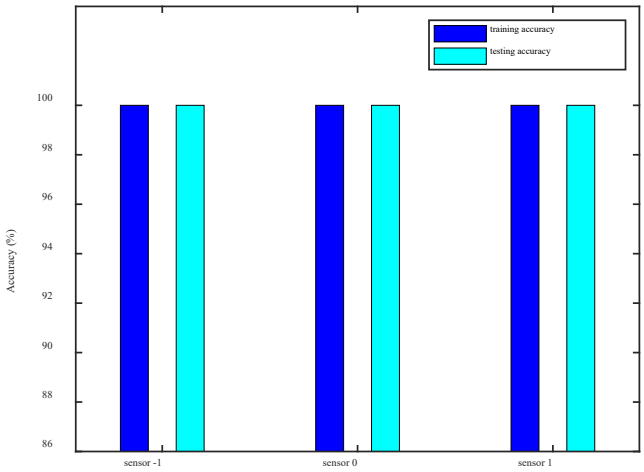

Figure 12. Comparison of quantitative damage evaluation accuracy at different sensor locations.

4.1.3. Effect of the number of training datasets

To examine how many training datasets can deliver reliable networks for quantitative damage evaluation, we trained the SHMnet five times, with an increasing number of group datasets as training data, Group 1, 2, 3, 4, and 5. As shown in Table 1, Group 1 only with 11 datasets while Group 5 with 55 datasets. Figure 13 shows the damage evaluation testing accuracy results using different numbers of training datasets from sensor 0. It demonstrates that with Group 1 datasets as training, the damage evaluation testing accuracy was low, that is, only 13%. This is because the amount of training data is rare, which only has datasets of 90 kHz frequency scenario. With the increase of the training datasets, the testing accuracy increases dramatically. While using Group 4 and Group 5 datasets as training, SHMnet can achieve over 90% damage evaluation testing accuracy and achieve 100% when Group 5 was used, which means that more datasets can lead to a model with better generalization ability. This may suggest that for future studies, at least Group 4 datasets are necessary to achieve optimal damage evaluation results. If we aim for 100% quantitative damage evaluation accuracy, at least 55 tests are needed.

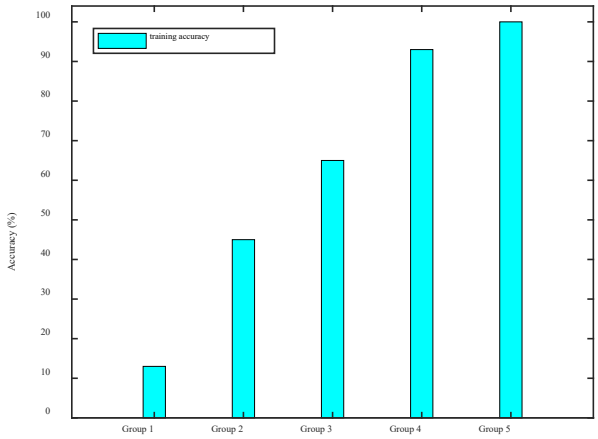

Figure 13. Quantitative damage evaluation accuracy using the different number of training datasets at sensor 0.

4.1.4. Quantitative damage evaluation results

After optimization, as shown in Figure 14, we can obtain the GW-SHMnet by setting the convolutional block number as 3, using any sensor of Passive PA and Group 4 or above quantity of datasets. Figure 15 plots the histories of both accuracy and loss on the training and testing datasets during the 1000 epochs of training for the case of 3 convolutional blocks. In the 0-500 epoch, the loss history decreases rapidly to converge to 0, while the accuracy history increases rapidly to converge to 100%. In the 500-1000 epoch, both loss and accuracy history stabilize with only slight fluctuations. The loss and accuracy of training and testing processes are close to each other throughout the whole training history. This indicates that the actual classification performance meets the expectations. It is concluded that GW-SHMnet can be used to assess

local damage in curved plates based on PAGW monitoring data.

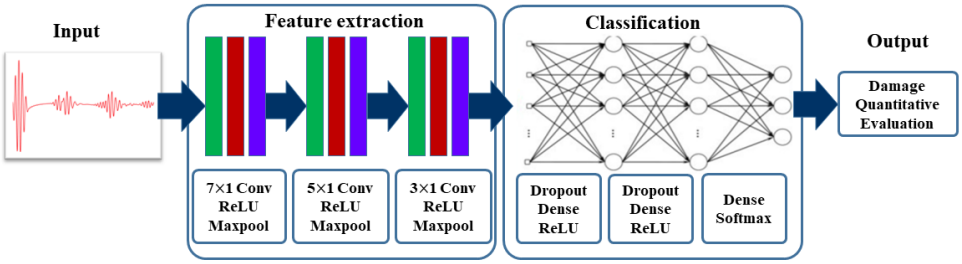

Figure 14. The framework of GW-SHMnet.

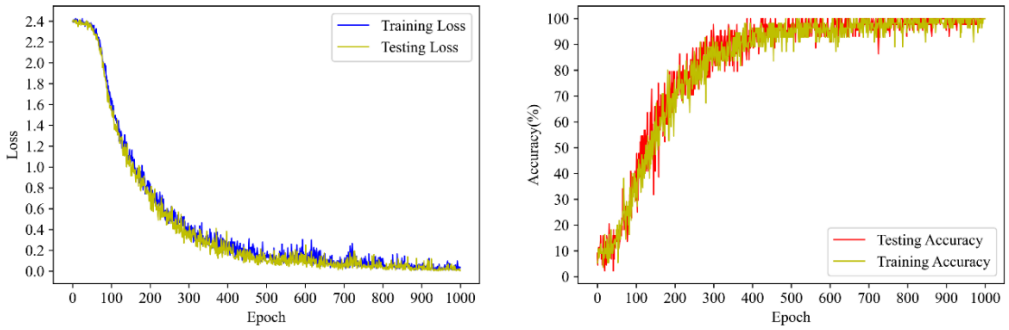

(a) **(b)**

Figure 15. Histories of (a) accuracy and (b) loss obtained during the 1000 epochs of training by GW-SHMnet.

4.2. *Results of the curve-fitting approach*

To compare with the results of the proposed approach, we developed a traditional curve-fitting approach. Here, the amplitudes of back-scattered CLT_0 of 99 different scenarios were extracted. The extracting method is to read the maximum amplitude of the backscattered CLT_0 wave packet in the synthetic difference signal. The results are presented in Table 4. From any column of Table 4, we can find that the amplitude of the reflected wave increases as the width of the damage increases. To evaluate the damage size, polynomial equations were used to fit curves to describe the relationship between the damage width and the amplitude of back-scattered CLT_0.

Table 4. The amplitude of back-scattered CLT_0 under 99 different scenarios

Amplitude	90 kHz **(1)**	92.5 kHz **(6)**	95 kHz **(2)**	97.5 kHz **(7)**	100 kHz **(3)**	102.5 kHz **(8)**	105 kHz **(4)**	107.5 kHz **(9)**	110 kHz **(5)**
Dm=0mm	0	0	0	0	0	0	0	0	0
Dm=5mm	0.011	0.010	0.011	0.011	0.012	0.014	0.016	0.018	0.020
Dm=10mm	0.066	0.075	0.085	0.095	0.104	0.113	0.121	0.127	0.132
Dm=15mm	0.131	0.142	0.151	0.161	0.171	0.179	0.185	0.188	0.190
Dm=20mm	0.167	0.178	0.189	0.203	0.214	0.223	0.229	0.233	0.235
Dm=25mm	0.198	0.219	0.237	0.255	0.271	0.283	0.292	0.297	0.300
Dm=30mm	0.250	0.268	0.285	0.305	0.322	0.335	0.342	0.346	0.347
Dm=35mm	0.282	0.300	0.319	0.340	0.358	0.371	0.378	0.382	0.380
Dm=40mm	0.320	0.340	0.358	0.380	0.399	0.413	0.421	0.424	0.422
Dm=45mm	0.342	0.364	0.381	0.405	0.424	0.437	0.445	0.446	0.443

Dm=50mm	0.351	0.371	0.390	0.414	0.432	0.444	0.450	0.450	0.446

Firstly, for an excitation frequency of 90 kHz, we fit a curve as shown in Figure 16 (a). Considering sufficient datasets are needed to fit (train) and test curves, we averaged the data in columns 1, 2, 3, 4, and 5 to fit the quadratic polynomial curve (viz. Figure 16 (b)), and averaged the data in columns 6, 7, 8, and 9 to test the accuracy of the model.

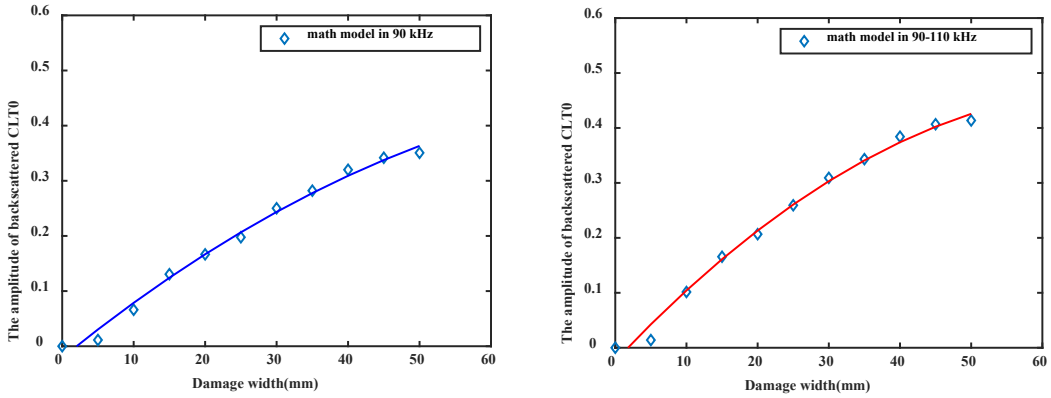

(a) (b)

Figure 16. (a) The quadratic polynomial fitting curve for 90 kHz; (b) Quadratic polynomial fitting curve for 90-110 kHz.

For Figure 16 (a), to test the accuracy of this fitted curve, we first calculated the difference between the data in 90 kHz scenarios and the corresponding values of the fitted curve, which is considered the training accuracy of the model. Secondly, we used the data in 92.5 kHz scenarios to compare with the corresponding data of the fitted curve and calculated their difference, which is assumed as the testing accuracy. According to the assumption mentioned above, the training accuracy and the testing accuracy can be calculated according to Equation (6) and Equation (7), respectively.

$$A_{training} = \frac{1}{N}\sum_{i=1}^{N}\left[1-\frac{\sqrt{\left(V_{f90}(i)-V_{FC90}(i)\right)^2}}{V_{FC90}(i)}\right]\times 100\% \quad (6)$$

$$A_{testing} = \frac{1}{N}\sum_{i=1}^{N}\left[1-\frac{\sqrt{\left(V_{f92.5}(i)-V_{FC90}(i)\right)^2}}{V_{FC90}(i)}\right]\times 100\% \quad (7)$$

$A_{training}$ and $A_{testing}$ refer to the training accuracy and the testing accuracy, respectively. N is the number of damage size scenarios, that is, 11 in this study. $V_{f90}(i)$ refers to the amplitude of back-scattered CLT_0 at 90 kHz excitation frequency for the i^{th} damage size scenarios. Similarly, $V_{FC90}(i)$ means the amplitude of back-scattered CLT_0 corresponding to the i^{th} damage size scenario of the fitted curve at 90 kHz excitation frequency.

For Figure 16 (b), we use the averaged data of columns 1, 2, 3, 4, and 5 ($V_{f\_average\_1,2,3,4,5}$), and the averaged data of columns 6, 7, 8, and 9 ($V_{f\_average\_6,7,8,9}$) to test the training and testing

accuracy of the fitted curves, respectively. Therefore, the training accuracy and the testing accuracy can be calculated according to Equation (8) and Equation (9). $V_{FC\_average\_1,2,3,4,5}(i)$ means the amplitude of back-scattered CLT_0 corresponding to the i^{th} damage size scenario of the fitted curve at 90, 95, 100, 105, and 110 kHz excitation frequency. $V_{FC\_average\_6,7,8,9}(i)$ means the amplitude of back-scattered CLT_0 corresponding to the i^{th} damage size scenario of the fitted curve at 92.5, 97.5, 102.5, and 107.5 kHz excitation frequency. Moreover, the order of polynomials can be optimized while fitting curves. Hence, in Table 5, we discuss the training and testing accuracy of the fitted curves using polynomials from 1 to 10.

$$A_{training} = \frac{1}{N}\sum_{i=1}^{N}\left[1-\frac{\sqrt{\left(V_{f\_average\_1,2,3,4,5}(i)-V_{FC\_average\_1,2,3,4,5}(i)\right)^2}}{V_{FC\_average\_1,2,3,4,5}(i)}\right]\times 100\% \quad (8)$$

$$A_{testing} = \frac{1}{N}\sum_{i=1}^{N}\left[1-\frac{\sqrt{\left(V_{f\_average\_6,7,8,9}(i)-V_{FC\_average\_6,7,8,9}(i)\right)^2}}{V_{FC\_average\_6,7,8,9}(i)}\right]\times 100\% \quad (9)$$

Table 5. Training and testing accuracy of the fitted curve using polynomials from 1 to 10 times.

Accuracy (%)		1st	2nd	3rd	4th	5th	6th	7th	8th	9th	10th
90 kHz	train	78.52	81.73	82.73	83.16	86.21	88.22	87.65	89.38	90.15	90.91
	test	75.07	78.67	78.13	78.23	80.78	84.50	84.06	84.32	83.62	83.76
90-110 kHz	train	78.47	83.13	83.24	82.70	84.16	87.18	90.03	89.81	90.90	90.91
	test	77.83	82.62	82.46	82.44	83.55	86.35	89.05	89.60	89.40	89.40

From Table 5, it can be found that the fitted curve is at least 75% accurate. As the order of polynomials increases, the accuracy of training and testing gradually improves, up to about 91%. However, when the order of polynomials is extremely high, the fitted curves will lose the capability of generalization. For the fitted curve of 90 kHz scenarios, the datasets could only reach a maximum of 90% accuracy using 10^{th} polynomials. When this fitted curve was tested with 92.5 kHz datasets, it was found that the maximum accuracy was about 84.5%. This indicates that the fitted curve of 90 kHz does not work well for datasets from other excitation frequencies. For the 90-110 kHz fitted curves, training, and test accuracy are very close to the highest about 90%, which happens in the 10^{th} polynomial fitted curve (viz. Figure 17(b)). Although the 10^{th} polynomial fitted curves always resulted in improved accuracy for both training and testing, the curves became unsmooth and overfitted, which made these curves lose generalizable. Therefore, we can conclude that the fitted curves have the potential to describe the relationship between damage width and back-scattered CLT_0 at different frequencies, but the training and testing accuracy and the capability of generalization need to be improved.

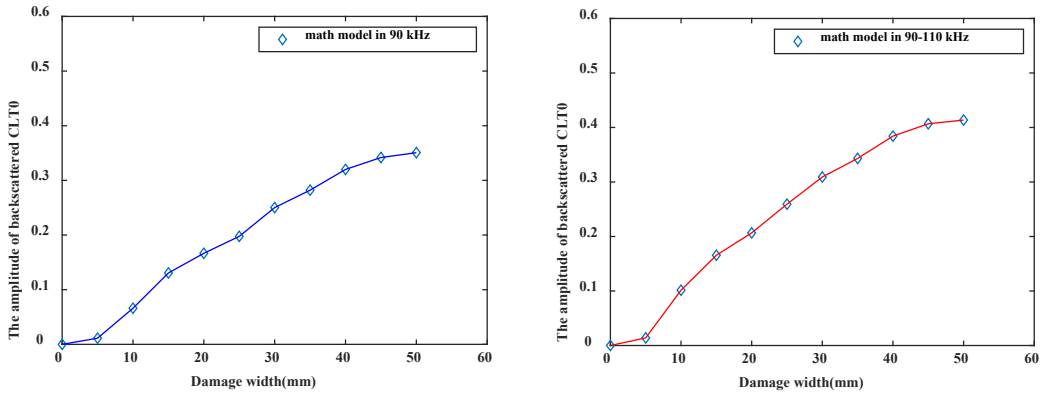

(a) (b)

Figure 17. (a) 10th polynomial fitted curve for 90 kHz; (b) 10th polynomial fitted curve for 90-110 kHz.

4.3. *Feasibility studies*

4.3.1. Robustness of the algorithm

In this subsection, the robustness of the proposed GW-SHMnet is tested. It was first trained by Group 5 datasets from sensor 0 of Passive PA under 11 scenarios. We then added different levels of Gaussian noise, which is used to simulate the effects of environmental noise and inhomogeneous material properties on the signal, onto the testing data and used the trained model to quantify damage size. We illustrate the difference between the original test data and that with 10% and 50% noise levels in Figure 18. It can be seen that with 50% noise, the signal data becomes significantly different, while 10% noise does not change the original signal much.

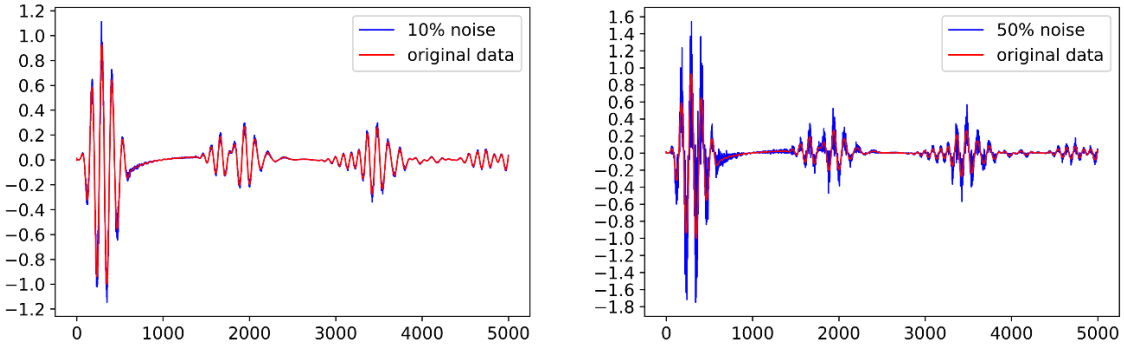

Figure 18. illustration of the original data and the data with different noise levels: (a) 10%; (b) 50%.

Note that the goal of the simulations was to create a benchmark dataset to test GW-SHMnet's ability to evaluate the damage size under different excitation frequencies. However, in practice, the difficulty of detection will mostly depend on the available signal-to-noise ratio (SNR) of the measurements. Therefore, to test GW-SHMnet at increasing levels of difficulty, five different levels of noise were added in post-processing by superposition to the simulation results.

To achieve reliable results, we implemented 30 repeated tests on the quantitative damage

evaluation using the data with 20%, 40%, 60%, 80%, and 100% Gaussian noises. The statistical results are summarized in Table 5 which indicates that the quantitative evaluation of damage using GW-SHMnet is reliable with an accuracy of more than 98% and a standard deviation of 0.71% in the case of 60% noise of the test data. Even in the case of 100% noise, the accuracy can reach 95%.

Table 6. Average results when random Gaussian noise with distinct levels were added to the testing data with 30 repeated tests.

Noise level (%)	20	40	60	80	100
Mean ±SD	99.25%± 0.49%	99.04%± 0.48%	98.41%± 0.71%	97.54%± 0.57%	95.37%± 0.71%

SD: standard deviation

4.3.2. Comparisons

Comparing the results of the proposed approach and that of the curve-fitting approach, the effectiveness, efficiency, and robustness of GW-SHMnet are advantageous. Especially, the overall accuracy of GW-SHMnet by using 'Group 5' data from any one sensor can achieve 100%, and it is over 95% even by adding 60% Gaussian noise to the testing data. In contrast, the maximum accuracy of the conventional curve-fitting approach is around 90%. Moreover, for scenarios with different damage size, the extraction of the amplitude of back-scattered CLT_0 rely on the manually synthesized difference signals from three sensors of Passive PA. Hence, evaluating the damage size is rather complicated by using the curve-fitting approach than the proposed approach. Therefore, it is recommended to use GW-SHMnet to realize quantitative damage evaluation of curved plates in practice.

4.3.3. Discussions

It should be noted that the present study used a cylindrical curved plate to assess the performance of the proposed approach. For real structures, the curve may be more complex, which may lead to more noisy wave propagation signals. Nevertheless, the proposed quantitative damage evaluation framework shown in Figure 1 can still work, as long as the numerical models can accurately represent wave propagation in the plates. Numerical simulations of more complex plates, such as wind turbine blades, are out of the scope of this study but will be our future work.

Theoretically, damage of any shape will obstruct the forward propagation of PAGW and cause proportional damage reflected wave. The larger the size perpendicular to the direction of PAGW propagation, the greater the extent of the wave that will be reflected. Therefore, the proposed method is promising to identify damage with irregular shapes. The applicability of the proposed method under different shapes of damage, such as triangles/circles/trapezoids, is

worthwhile investigating in the future.

5. Conclusions

This paper proposed a novel damage evaluation approach to quantitatively assess the damage size, and its performance was compared with the conventional curve-fitting method. The focusing theory of the PAGW was implemented as the pre-processing procedure of non-destructive testing of the curved plate for its wave energy focusing/steering capability to amplify the damage reflections. Damage-reflected waveform, the amplitude of back-scattered CLT_0, was found and extracted in both numerical and experimental studies. The experimental results demonstrated that the FE model can be used to generate the database for the proposed approach. Based on the FE numerical dataset, a state-of-the-art network was optimized to generate GW-SHMnet, together with fitted polynomial curves. The quantitative damage evaluation results demonstrate:

1. Automatic damage evaluation of curved plates can be achieved by using the proposed approach, which integrates the advantages of the PAGW and deep learning algorithm.

2. GW-SHMnet is effective and efficient in quantitative damage evaluation, with 100% accuracy in laboratory test cases, using 3 convolutional blocks and at least 5 group test data from any one sensor as training. Meanwhile, GW-SHMnet is robust when the testing data are smeared with Gaussian noise. Even under 100% Gaussian noise, the quantitative damage evaluation can achieve an accuracy of over 95%.

3. The classic curve-fitting method evaluates the damage size by establishing the relationship between the damage-reflected waveform and damage size successfully. Its maximum accuracy is up to about 91%. Compared with the traditional curve-fitting method, the accuracy of the deep learning approach has improved by about 10% in our study.

Overall, our results demonstrate the potential of the proposed approach as an effective tool for quantitative damage evaluation by incorporating a state-of-the-art network with high-precision PAGW. This non-invasive, effective, and accurate damage evaluation method provides opportunities for diagnosing and assessing a broad range of curved plates in a true phased-array control format. Future research efforts may be placed on (1) increasing the number of PAGW elements with advanced electronic control to realize the automatic scanning of plates in practice; and (2) the application of the proposed approach to more complex curved plates, such as those with irregular damage shapes.

Declaration of Competing Interest

The authors declare that they have no known competing financial interests or personal relationships that could have appeared to influence the work reported in this paper.

Authorship Contribution Statement

Qi Yuan: Conceptualization, Methodology, Investigation, Software, Formal analysis, Experiment, Writing - original draft, Writing - review & editing, Data curation, Visualization. **Ying Wang:** Conceptualization, Methodology, Supervision, Writing - review & editing, Funding acquisition. **Zhongqing Su:** Methodology, Supervision. **Tong Zhang:** Conceptualization, Methodology, Validation, Writing - review & editing.

Acknowledgment

The authors would like to thank Shenzhen Science, Technology and Innovation Commission, China, for the financial support through Grant JCYJ20210324124212034.

References

[1] Y. Wang, X. Zhu, H. Hao, J. Ou, Guided wave propagation and spectral element method for debonding damage assessment in RC structures, Journal of Sound and Vibration, 324 (2009) 751-772.
[2] S. Zhang, R. Shen, K. Dai, L. Wang, G. De Roeck, G. Lombaert, A methodology for cable damage identification based on wave decomposition, Journal of Sound and Vibration, 442 (2019) 527-551.
[3] M. Palacz, A. Zak, M. Krawczuk, FEM-Based Wave Propagation Modelling for SHM: Certain Numerical Issues in 1D Structures, Materials (Basel), 13 (2020).
[4] B. Lei, N. Wang, P. Xu, G. Song, New Crack Detection Method for Bridge Inspection Using UAV Incorporating Image Processing, Journal of Aerospace Engineering, 31 (2018).
[5] Y. Shao, L. Zeng, J. Lin, Damage detection of thick plates using trailing pulses at large frequency-thickness products, Applied Acoustics, 174 (2021).
[6] P. WLoveday, C.S. Long, D.A. Ramatlo, Ultrasonic guided wave monitoring of an operational rail track, Structural Health Monitoring, 19 (2019) 1666-1684.
[7] Y. Lu, L. Ye, Z. Su, Crack identification in aluminium plates using Lamb wave signals of a PZT sensor network, Smart Materials and Structures, 15 (2006) 839-849.
[8] S. Mariani, Q. Rendu, M. Urbani, C. Sbarufatti, Causal dilated convolutional neural networks for automatic inspection of ultrasonic signals in non-destructive evaluation and structural health monitoring, Mechanical Systems and Signal Processing, 157 (2021).
[9] S.J. LW, Fundamentals of ultrasonic phased arrays, Modern Physics Letters B, 22(11):917-21. (2008).

[10] L. Yu, Z. Tian, Guided wave phased array beamforming and imaging in composite plates, Ultrasonics, 68 (2016) 43-53.
[11] P. Huthwaite, Evaluation of inversion approaches for guided wave thickness mapping, Proceedings of the Royal Society A: Mathematical, Physical and Engineering Sciences, 470 (2014).
[12] P. Belanger, P. Cawley, F. Simonetti, Guided wave diffraction tomography within the born approximation, IEEE transactions on ultrasonics, ferroelectrics, and frequency control, 57 (2010) 1405-1418.
[13] J. Rao, M. Ratassepp, Z. Fan, Guided Wave Tomography Based on Full-Waveform Inversion, IEEE Trans Ultrason Ferroelectr Freq Control, 63 (2016) 737-745.
[14] T.R. Hay, R.L. Royer, H. Gao, X. Zhao, J.L. Rose, A comparison of embedded sensor Lamb wave ultrasonic tomography approaches for material loss detection, Smart Materials and Structures, 15 (2006) 946-951.
[15] G. Giridhara, V.T. Rathod, S. Naik, D. Roy Mahapatra, S. Gopalakrishnan, Rapid localization of damage using a circular sensor array and Lamb wave based triangulation, Mechanical Systems and Signal Processing, 24 (2010) 2929-2946.
[16] X. Zhao, R.L. Royer, S.E. Owens, J.L. Rose, Ultrasonic Lamb wave tomography in structural health monitoring, Smart Materials and Structures, 20 (2011).
[17] G. Lu, Y. Li, T. Wang, H. Xiao, L. Huo, G. Song, A multi-delay-and-sum imaging algorithm for damage detection using piezoceramic transducers, Journal of Intelligent Material Systems and Structures, 28 (2016) 1150-1159.
[18] Y. Lu, L. Ye, Z. Su, C. Yang, Quantitative assessment of through-thickness crack size based on Lamb wave scattering in aluminium plates, NDT & E International, 41 (2008) 59-68.
[19] J. Yang, Y. Su, Y. Liao, P. Zhou, L. Xu, Z. Su, Ultrasound tomography for health monitoring of carbon fibre–reinforced polymers using implanted nanocomposite sensor networks and enhanced reconstruction algorithm for the probabilistic inspection of damage imaging, Structural Health Monitoring, 21 (2021) 1110-1122.
[20] H. Song, Y. Yang, Noncontact super-resolution guided wave array imaging of subwavelength defects using a multiscale deep learning approach, Structural Health Monitoring, 20 (2020) 1904-1923.
[21] M.M. Bahador, A. Zaimbashi, R. Rahgozar, Three-stage Lamb-wave-based damage localization algorithm in plate-like structures for structural health monitoring applications, Signal Processing, 168 (2020).
[22] M.M. Malatesta, D. Bogomolov, M. Messina, D. D'Ippolito, N. Testoni, L. De Marchi, A. Marzani, The Delay Multiply and Sum Algorithm for Lamb Waves Based Structural Health Monitoring, European Workshop on Structural Health Monitoring, 2021, pp. 657-666.
[23] S. Zhang, C.M. Li, W. Ye, Damage localization in plate-like structures using time-varying feature and one-dimensional convolutional neural network, Mechanical Systems and Signal Processing, 147 (2021).
[24] M. Demetgul, V.Y. Senyurek, R. Uyandik, I.N. Tansel, O. Yazicioglu, Evaluation of the health of riveted joints with active and passive structural health monitoring techniques, Measurement, 69 (2015) 42-51.
[25] Q. Yuan, B. Kato, K. Fan, Y. Wang, Phased array guided wave propagation in curved plates, Mechanical Systems and Signal Processing, 185 (2023).

[26] M. Ghriba, M. Rébillata, G.V.d. Rochesb, N. Mechbal, Automatic damage type classification and severity quantification using signal based and nonlinear model based damage sensitive features, Journal of Process Control, 83 (2019) 136-146.
[27] Y.F. Lee, Y. Lu, Advanced numerical simulations considering crack orientation for fatigue damage quantification using nonlinear guided waves, Ultrasonics, 124 (2022) 106738.
[28] H. Mei, V. Giurgiutiu, Guided wave excitation and propagation in damped composite plates, Structural Health Monitoring, 18 (2018) 690-714.
[29] M. Corbetta, A. Saxena, M. Giglio, K. Goebel, An investigation of strain energy release rate models for real-time prognosis of fiber-reinforced laminates, Composite Structures, 165 (2017) 99-114.
[30] N. Yue, M.H. Aliabadi, A scalable data-driven approach to temperature baseline reconstruction for guided wave structural health monitoring of anisotropic carbon-fibre-reinforced polymer structures, Structural Health Monitoring, 19 (2019) 1487-1506.
[31] Z. Su, L. Ye, Lamb wave-based quantitative identification of delamination in CF/EP composite structures using artificial neural algorithm, Composite Structures, 66 (2004) 627-637.
[32] A. Malekloo, E. Ozer, M. AlHamaydeh, M. Girolami, Machine learning and structural health monitoring overview with emerging technology and high-dimensional data source highlights, Structural Health Monitoring, (2022).
[33] J. Rao, F. Yang, H. Mo, S. Kollmannsberger, E. Rank, Quantitative reconstruction of defects in multi-layered bonded composites using fully convolutional network-based ultrasonic inversion, Journal of Sound and Vibration, 542 (2023).
[34] T. Zhang, S. Biswal, Y. Wang, SHMnet: Condition assessment of bolted connection with beyond human-level performance, Structural Health Monitoring, 19 (2019) 1188-1201.
[35] W. Wang, H. Zhang, J.P. Lynch, C.E.S. Cesnik, H. Li, Experimental and numerical validation of guided wave phased arrays integrated within standard data acquisition systems for structural health monitoring, Structural Control and Health Monitoring, 25 (2018).
[36] D.F. Hesser, S. Mostafavi, G.K. Kocur, B. Markert, Identification of acoustic emission sources for structural health monitoring applications based on convolutional neural networks and deep transfer learning, Neurocomputing, 453 (2021) 1-12.
[37] J.L. Rose, Ultrasonic guided waves in solid media, Cambridge university press, UK, 2004.
[38] M.L.B. Pavlakovic, DISPERSE User's Manual, Non-Destructive Testing Laboratory, Department of Mechanical Engineering, Imperial College London, UK, 2013.
[39] J. Park, Y. Cho, A study on guided wave tomographic imaging for defects on a curved structure, Journal of Visualization, 22 (2019) 1081-1092.
[40] S. Zhang, W. Fan, An efficient semi-analytical formulation for the Lamb-like waves in layered waveguides based on global discretization, Computers & Structures, 249 (2021).
[41] B.R. Mace, E. Manconi, Modeling wave propagation in two-dimensional structures using finite element analysis, Journal of Sound and Vibration, 318 (2008) 884-902.